Supporting Information

Dual functions of CO_2 molecular activation and 4*f* levels as electron transport bridge in erbium single atom composite photocatalysts therefore enhancing visible-light photoactivities

Qiuyu Chen,[‡a] Guoyang Gao,[‡a] Yanzhou Zhang,[a] Yini li,[a] Hongyang Zhu,*[b] Peifen Zhu,[c] Yang Qu,[a] Guofeng Wang*[a] and Weiping Qin[d]

[a]Key Laboratory of Functional Inorganic Material Chemistry, Ministry of Education, School of Chemistry and Materials Science, Heilongjiang University, Harbin 150080, China

[b]School of Physics and Electronic Engineering, Linyi University, Linyi 276005, China

[c]Department of Physics and Engineering Physics, The University of Tulsa, Tulsa, OK 74104, USA

[d] College of Electronic Science and Engineering, Jilin University,Changchun 130012, China

*Correspondence: 2010070@hlju.edu.cn (G. Wang); zhuhongyang@lyu.edu.cn (H. Zhu)

[‡]Qiuyu Chen and Guoyang Gao contributed equally to this work

1. Materials and characterizations

Chemicals: All reagents and solvents, including analytical-grade $Sr(NO_3)_2$, $Ti(OC_4H_9)_4$, $Er(NO_3)_3 \cdot 6H_2O$, PEG-200, NaOH, acetone, CH_3COOH, melamine, ethanol, and methanol, were used as received without further purification. It is noted that the obtained samples of STO:Er^{3+}/CN composed of 1, 3, 5, 7, 10, 20, and 50% STO:Er^{3+} (wt%) were named as 1-STO:Er^{3+}/CN, 3-STO:Er^{3+}/CN, 5-STO:Er^{3+}/CN, 7-STO:Er^{3+}/CN, 10-STO:Er^{3+}/CN, 20-STO:Er^{3+}/CN, and 50-STO:Er^{3+}/CN, respectively.

***Characterization*:** X-ray diffraction (XRD) patterns were recorded on a Bruker D8 Advance diffractometer equipped with Cu *Kα* radiation (λ = 1.5406 Å, 40 kV, 40 mA). The surface elemental information was analyzed by X-ray photoelectron spectroscopy (XPS) performed on a Kratos-AXIS ULTRA DLD apparatus with an Al (mono) X-ray source. Inductively coupled plasma (ICP-OES) measurement was performed using the Thermo Scientific iCAP 7400 ICP-OES. The morphology of the sample was characterized using scanning electron microscopy (SEM, Hitachi, S-4800), transmission electron microscopy (TEM, JEOL, JEM-2100) and aberration-corrected high-angle annular dark-field scanning transmission electron microscopy (AC HAADF-STEM, JEM-ARM300F). Nitrogen adsorption-desorption isotherms were collected using a Tristar II 3020 surface area and porosity analyzer (Micromeritics). The Fourier transform infrared (FT-IR) spectra were recorded with KBr pellets in the range of 4000-400 cm^{-1} on a Perkin-Elmer Spectrum One spectrometer. UV-vis diffuse reflectance spectroscopy (UV-vis DRS) was performed using a spectrophotometer (SHIMADZU UV-2550), and $BaSO_4$ was used as the background. Photoluminescence (PL) spectra were measured using a Hitachi F-4600 fluorescence spectrophotometer equipped with a 150W Xe lamp at room temperature. Photoelectrochemical measurements (PEC) were characterized with a computer-controlled CHI-660 electrochemical workstation (Chenhua Instrument, Shanghai, China) with a 300W Xe arc lamp as a light source.

Photoelectrochemical measurement: Photocurrent measurements were performed using a three-electrode configuration with the sample film as the working electrode, saturated Ag/AgCl as the reference electrode, and platinum foil as the counter electrode. The working electrode films were prepared via the doctor-blade method using a thin glass rod to roll a paste onto the fluorine-doped tin oxide (FTO)-coated glass to form a film (1 cm × 1 cm). A 0.5 M Na_2SO_4 aqueous solution was used as the electrolyte. Finally, the electrode was dried at room temperature and annealed at 150 °C for 2 h under N_2 atmosphere.

The paste was prepared as follows: 0.1 g of the photocatalyst powder was dispersed to 1 mL isopropyl alcohol and kept under vigorous stirring, subsequently, 0.05 g Macrogol-2000 and 0.05 mL acetylacetone were added to the above solution, respectively. The obtained solution was kept under adequately stirring for a week.

Hydroxyl radical measurement: Coumarin fluorescent method was used to detect the amount of hydroxyl radical (·OH) produced, typically, 0.05 g product was dissolved in 40 mL coumarin aqueous solution (0.001 M), then the solution was stirred for 10 min adequately and illuminated with a 300 W high-pressure Xenon lamp for 1 h. Finally, the obtained solution was separated by centrifugation and transferred into a Pyrex glass cell. And analyzed with the fluorescence measurement of 7-hydroxycoumarinat using a spectrofluorometer.

Photocatalytic Measurement: The photocatalytic for CO_2 reduction experiments were performed at room temperature in a 100 mL volume of cylindrical steel reactor and the irradiation area was 3.5 cm^2. The visible light was provided by a 300 W Xenon lamp (PLSSXE300/300UV, PerfectLight, Beijing) coupled with a 420 nm cut-off filter. In a typical experiment, 0.02 g of photocatalyst powder was dispersed in either a pure water solution (4 mL) or a mixture of acetonitrile (3 mL), water (1mL), and triethanolamine (1 mL). The reaction vessel was evacuated by CO_2 for 40 min to remove air and to establish an adsorption and desorption balance before photocatalytic experiments. After light irradiation, gas evolved was analyzed using an online gas chromatograph (GC2002). All the photocatalytic reactions were repeated several times and the data used in this article were the average value.

2. Computational Details

The first-principles calculations were performed based on density functional theory (DFT) implemented in the Vienna ab-initio simulation package (VASP).[1-3] The electron-ion interaction was described by the projector augmented wave (PAW) method.[4] The generalized gradient

approximation (GGA) with the Perdew-Burke-Ernzerhof (PBE) exchange-correlation functional was used in the calculations.[5] The band structure, partial density of states (PDOS), work function, and charge density difference were simulated with the plane-wave ultrasoft (PWUS) pseudopotential method as implemented in the MedeA-VASP.[6] The cutoff energy for the plane-wave expansion was set to 500 eV. For geometry optimization, the convergence criterion of total energy was 1.0×10^{-5} eV/atom. The spin-polarized magnetic calculation was used to do geometry optimization, electronic structure and optical property calculation. The spacing of k points were set to 0.199/Å. For bulk calculations, primitive cell of $SrTiO_3$ were considered with Γ-centered k-point grids of 8× 8 × 8. Furthermore, on-site Coulomb interactions are included for d orbital of Ti (U=2.5 eV) and f orbital of Er (U=6 eV) using GGA+U method. Electron localization function was obtained by using MedeA. The differential charge density (also called deformation charge density) was obtained by taking the difference between the self-consistent pseudo charge density and superposition of atomic charge densities. The real (ε_r) and imaginary (ε_i) parts of complex dielectric constants ($\varepsilon_{complex}$) were extracted from vasp calculation: $\varepsilon_{complex}(\omega) = \varepsilon_r(\omega) + i\varepsilon_i(\omega)$, where ω is the angular frequency of light. The complex optical conductivity was defined as $\sigma_{complex}(\omega) = \sigma_r(\omega) + i\sigma_i(\omega)$. The real part of optical conductivity was calculated as $\sigma_r(\omega) = \frac{\varepsilon_o \varepsilon_i \omega}{4\pi}$ and imaginary part of optical conductivity was calculated as $\sigma_i(\omega) = \frac{\varepsilon_o \varepsilon_r \omega}{4\pi}$, where ε_o is permittivity in free space. The complex refractive index was defined as $n_{complex}(\omega) = n(\omega) + ik(\omega)$. The real part of refractive index was calculated as $n(\omega) = \left[\left(\varepsilon_r^2 + \varepsilon_i^2\right)^{\frac{1}{2}} + \varepsilon_r^2\right]^{\frac{1}{2}}$ and the imaginary part of refractive index (extinction coefficient) was calculated as $k(\omega) = \left[\left(\varepsilon_r^2 + \varepsilon_i^2\right)^{\frac{1}{2}} - \varepsilon_r^2\right]^{\frac{1}{2}}$. The absorption coefficient was calculated as $\alpha_{abs}(\omega) = 2\frac{\omega k(\omega)}{c}$, where c is the speed of light in vacuum.

The construction of surfaces was done with MedeA.[6] For surface calculations, the 3 × 2 × 1 k-point was used to sample the surface Brillouin zone. Ground-state atomic geometry of the unit cell was obtained by minimizing the forces on the atoms to below 0.02 eV/Å. The force tolerance for the structure optimization is 0.02 eV/Å. The CO_2 adsorption energies (E_{ads}) were calculated by the following equation:

$$E_{ads} = E_{co2\text{-}sample} - (E_{sample} + E_{CO2}) \quad \text{(S1)}$$

Where $E_{co2\text{-}sample}$, E_{sample}, and E_{CO2} are the total energies of the CO_2 adsorbate-sample complex, the sample, and the CO_2, respectively. The work function of the surface was calculated according to the following equation:

$$\Phi = E_{vacuum} - E_F \quad \text{(S2)}$$

where E_{vacuum} and E_F represent the energy of a stationary electron in the vacuum near the surface and Fermi energy, respectively. It is noted that the Fermi energy is used as the zero of the energy scale. In addition, the density-derived electrostatic and chemical (DDEC) approach was used to calculate the net charge on each atom.[7,8]

3. The effect of the fluorescence quenching effect Er^{3+} ions on the electron transfer from CN to STO.

As discussed in the main text, both the radiative and nonradiative transition among the energy levels of Er^{3+} ions are not conducive to electron transfer from CN to STO. It is well known that the lifetime of an excited state of Er^{3+} ions is governed by a combination of probabilities for all possible radiative and nonradiative transitions. The nonradiative transition $^4G_{11/2} \rightarrow {}^2H_{9/2}$ of Er^{3+} ions also plays a key role in the radiative transition of Er^{3+} ions. The probability of nonradiative decay was found to be very dependent upon the proximity of lower energy levels. For the radiative transitions, it is well known that the electric-dipole transitions require a change in parity between initial and final states and therefore are forbidden between $4f^{11}$ states of the Er^{3+} ions. If the Er^{3+} ion resides in a

noncentrosymmetric static or dynamic crystal field, however, odd harmonics in the expansion of the crystalline potential can introduce a small admixture of opposite parity states from $4f^{11}5d$ state into the original $4f^{11}$ state and thereby electric-dipole transitions become allowed. The results photoluminescence spectrum of Er^{3+} ions (Figure 4h) indicated that the fluorescence quenching effect was observed for STO:Er^{3+}, and thus, Er^{3+} ions is very suitable as ET bridge from CN to STO. Here, it is widely accepted that PL intensity is directly related to the recombination of electron-hole pairs. And the stronger is the PL signal, the higher is the photogenerated charge recombination. The PL intensity of STO is low in Figure 4h, owing to the good crystalline, ordered cubic structure with less extrinsic defects of pure STO. The PL intensity of CN is significantly decreased after introducing STO:Er^{3+}.

4. Discussion for the photogenerated carrier lifetime.

The luminescence decay curves for the CN and 5-STO:Er^{3+}/CN were also carried out to evaluate the photogenerated carrier lifetime. Both attenuation curves were well fitted with a double exponential function as shown in Figure 4i, the average lifetime (τ) was determined using the formula $\tau = \sum_{i=1}^{2} A_i \tau_i^2 / \sum_{i=1}^{2} A_i \tau_i$. It is obvious that the carrier lifetime of CN and 5-STO:Er^{3+}/CN was calculated as 6157 ns and 6270 ns, respectively, indicating more effective electron-hole pair generation for 5-STO:Er^{3+}/CN sample.

5. Supplementary Figures and Tables.

Table S1. The total energies and optimized lattice parameters of STO, STO:Er^{3+}(16.6 mol%), and CN are calculated by employing the VASP code as described in the text.

Samples	a-axis (Å)	b-axis (Å)	c-axis (Å)	Volume (Å^3)	Etot (eV)
STO	3.941	3.941	3.941	61.22	-40.10
STO:Er^{3+}	3.905	3.905	3.904	59.52	-40.43
CN	4.76	4.76	6.35	124.71	-58.51

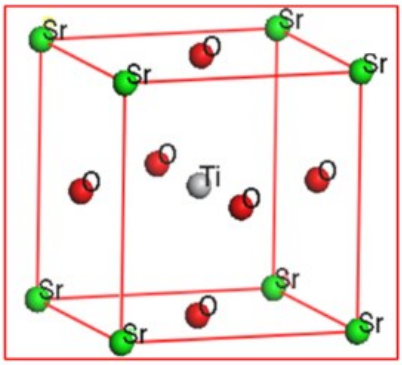

Figure S1. The optimized structure diagram of STO.

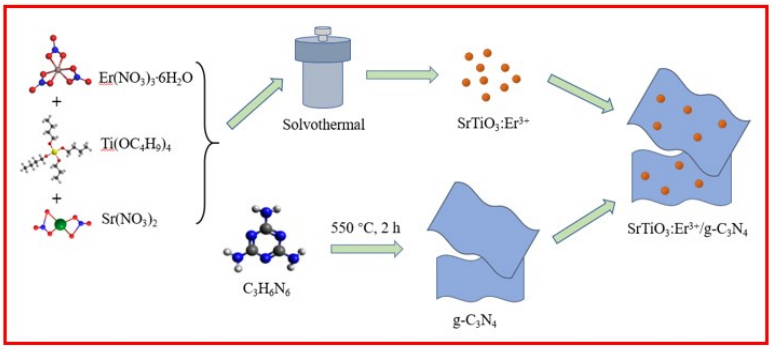

Figure S2. Synthesis route of STO:Er^{3+}/CN.

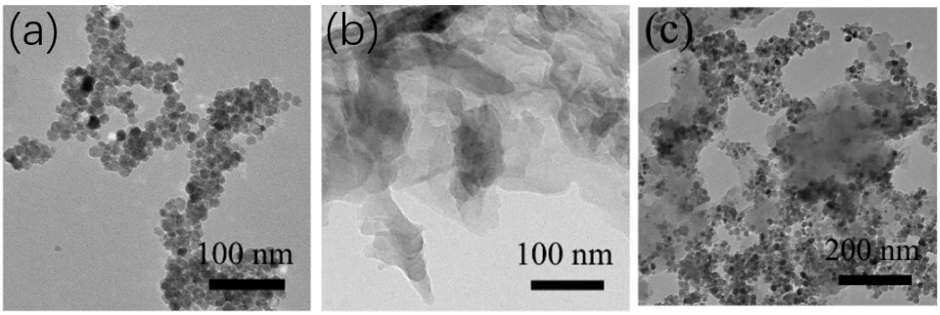

Figure S3. TEM images of (a) STO, (b) CN and (c) 50-STO:Er^{3+}/CN.

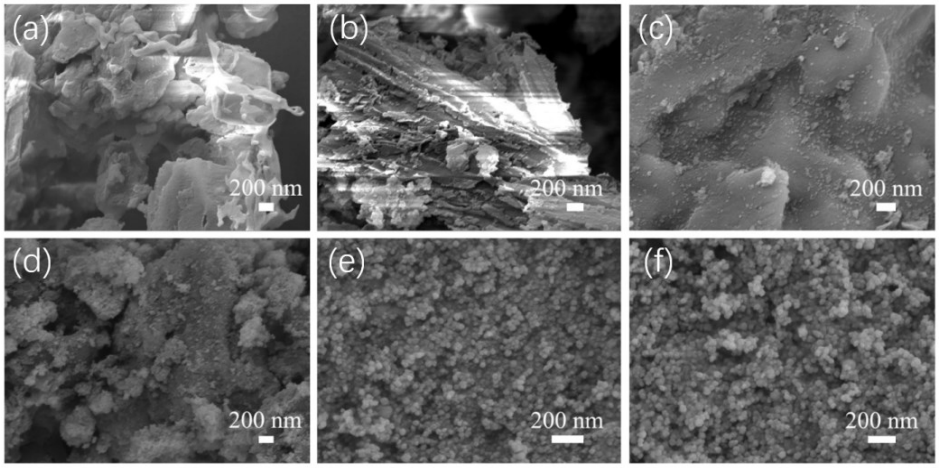

Figure S4. SEM images of (a) CN, (b) 5-STO:Er^{3+}/CN, (c) 10-STO:Er^{3+}/CN, (d) 50-STO:Er^{3+}/CN, (e) STO:Er^{3+}, and (f) STO.

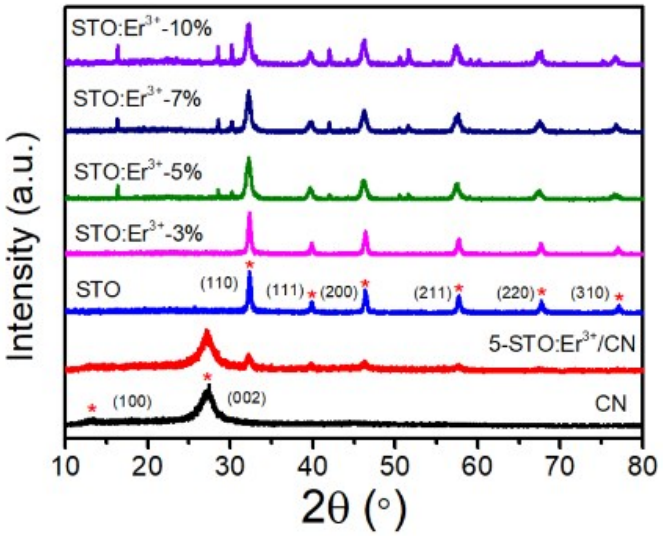

Figure S5. XRD patterns of samples.

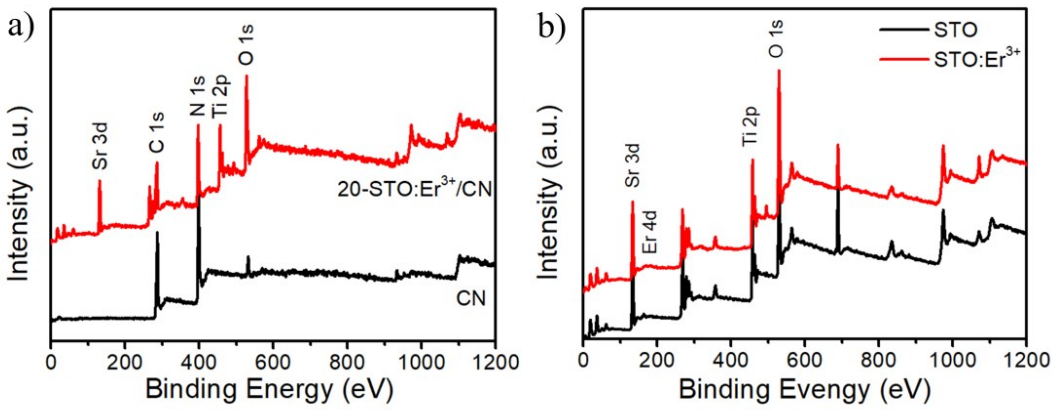

Figure S6. XPS survey spectra of different samples.

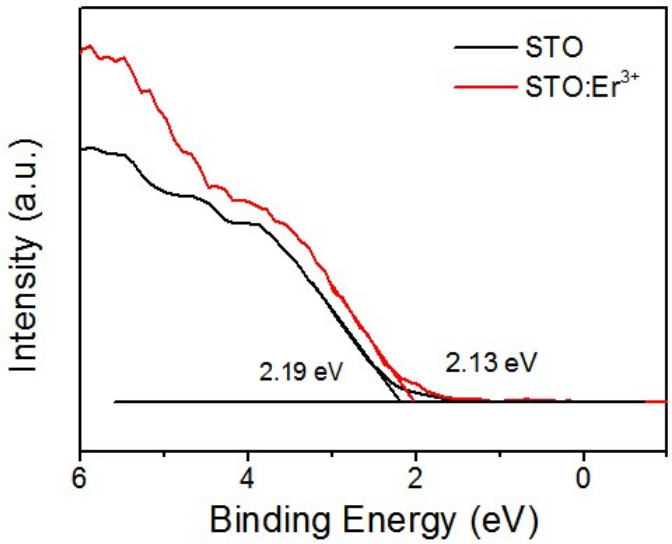

Figure S7. XPS valence band spectra of STO and STO:Er^{3+}.

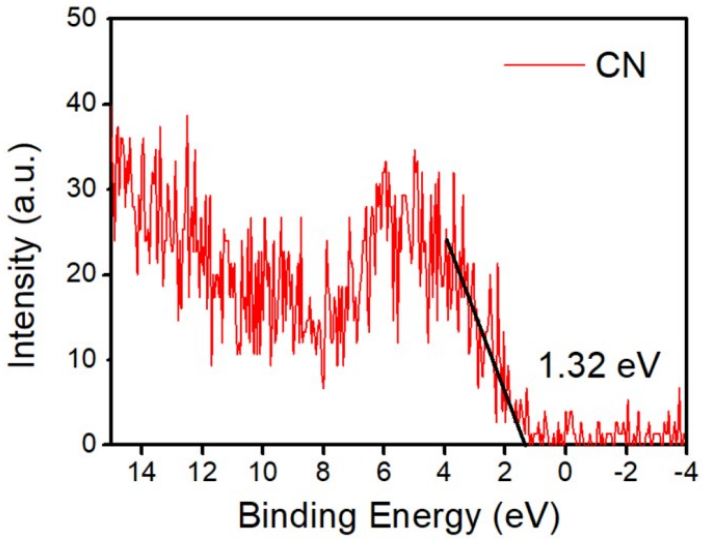

Figure S8. XPS valence band spectrum of CN.

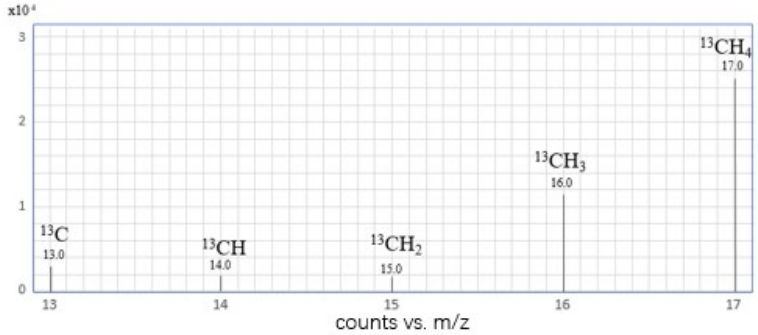

Figure S9. Mass spectra analyses of the carbon source of the evolved CH_4 in the photocatalytic reduction of $^{13}CO_2$.

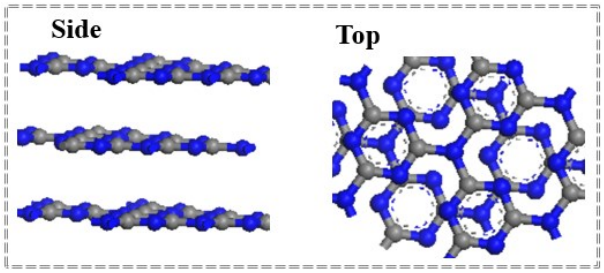

C_3N_4(001)

Figure S10. The optimized structure diagrams of CN (001).

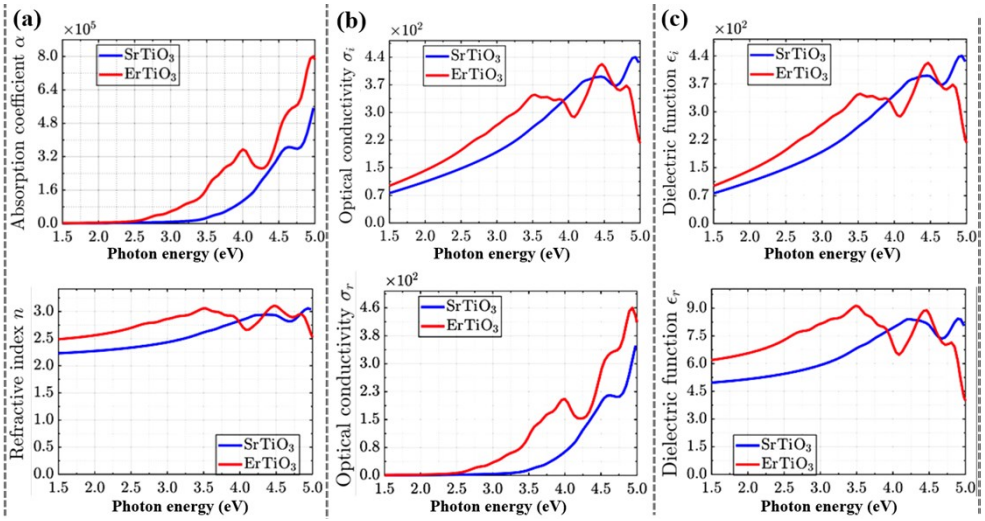

Figure S11. Theoretical simulation results of (a) absorption coefficient and refractive index, (b) optical conductivity, and (c) dielectric function.

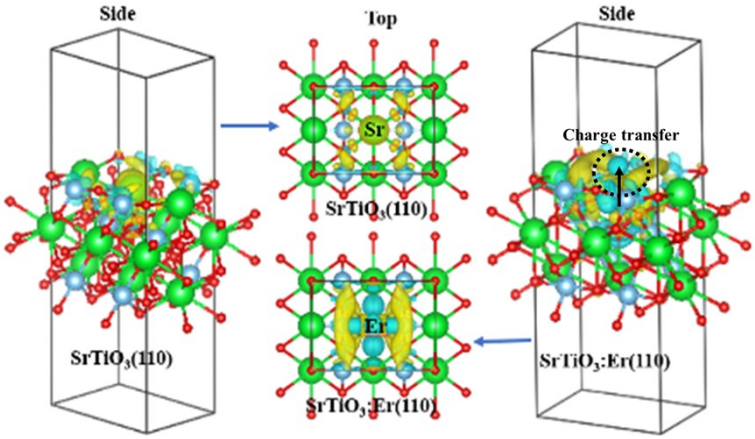

Figure S12. The effect Er^{3+} on the charge density difference around Er^{3+} in STO:Er^{3+} (110). The yellow and cyan surfaces correspond to the charge gain and charge loss, respectively.

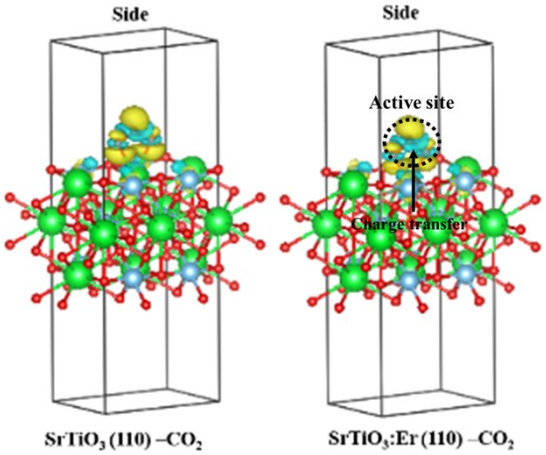

Figure S13. The effect Er^{3+} on the charge density difference around CO_2 in CO_2-STO:Er^{3+} (110). The yellow and cyan surfaces correspond to the charge gain and charge loss, respectively.

References

[1] G. Kresse, J. Hafner, Ab initio molecular dynamics for open-shell transition metals, *Phys. Rev. B* **1993**, *48*, 13115-13118.

[2] G. Kresse, J. Furthmüller, Efficiency of ab-initio total energy calculations for metals and semiconductors using a plane-wave basis set, Comput. *Mater. Sci.* **1996**, *6*, 15-50.

[3] G. Kresse, J. Furthmüller, Efficient iterative schemes for ab initio total-energy calculations using a plane-wave basis set, *Phys. Rev. B* **1996**, *54*, 11169-11186.

[4] G. Kresse, D. Joubert, From ultrasoft pseudopotentials to the projector augmented-wave method, *Phys. Rev. B* **1999**, *59*, 1758-1775.

[5] J. P. Perdew, K. Burke, M. Ernzerhof, Generalized Gradient Approximation Made Simple, *Phys. Rev. Lett.* **1996**, *77*, 3865-3868.

[6] https://www.materialsdesign.com/products.

[7] T. A. Manz, Introducing DDEC6 atomic population analysis: part 3. A comprehensive method to compute bond orders. *RSC Adv*. **2017**, *7*, 45552-45581.

[8] T. A. Manz and N. G. Limas, Introducing DDEC6 atomic population analysis: part 1. Charge partitioning theory and methodology. *RSC Advances* **2016**, *6*, 47771-47801.